applied optics

Generation of coherent and incoherent Airy beam arrays and experimental comparisons of their scintillation characteristics in atmospheric turbulence

Qiang Lu,[1,2,*] Shijie Gao,[1] Lei Sheng,[1] Jiabin Wu,[1] and Yanfeng Qiao[1]

[1]Changchun Institute of Optics, Fine Mechanics and Physics, Chinese Academy of Sciences, Dongnanhu Road 3888, Changchun 130033, China
[2]University of Chinese Academy of Sciences, Beijing 100049, China
*Corresponding author: luqiang52177@163.com

Received 13 February 2017; revised 2 April 2017; accepted 3 April 2017; posted 5 April 2017 (Doc. ID 286598); published 25 April 2017

We investigate, through numerical calculation and experiments, the incoherent combination of a 2D Airy beam array (ICCAB) and the coherent combination of a 2D Airy beam array (CCAB), respectively. Excellent experimental results are obtained for both ICCAB and CCAB. The on-axis scintillation indices of ICCAB and CCAB at the receiver plane in atmospheric turbulence are also compared experimentally. It is shown that ICCAB has a smaller scintillation index than that of CCAB in the same turbulent condition due to the coherence reduction of the constituent beamlets. The results obtained in this paper are useful for the development of beam propagation through atmosphere turbulence.

OCIS codes: (140.3298) Laser beam combining; (010.1330) Atmospheric turbulence; (090.1760) Computer holography.

https://doi.org/10.1364/AO.56.003750

1. INTRODUCTION

Since the first experimental demonstration of Airy beams within the context of optics in 2007 [1], this unique type of beam has been an active area of research in recent years that has included generation methods, trajectory control, and practical applications. It is well known that the one and two transverse dimension Airy beams have been generated by different approaches in the laboratory [2–6]. Following these laboratory approaches, the circular Airy beam has also been illustrated theoretically and experimentally [7–12]. Owing to its "diffraction-free," "self-healing," and "self-bending" features on propagation, Airy beams are widely applied to vacuum electron [13], optical trapping [14], microparticle clearing [15,16], surface plasmon polaritons [17], and free space optical communication [18].

Recently, it has been shown that Airy beams have a "self-healing feature" to retain the intensity profile during propagation in atmospheric turbulence [19]. This distinctive property suggests to researchers that Airy beams can be used for beam propagation in turbulence to provide some advantages, as the asymmetric transverse intensity characteristic of single 1D or 2D Airy beams is disadvantageous in some practical applications. Researchers have begun to transfer their attention to constituting a symmetric beam array through superimposing two or four single 1D or 2D Airy beams for compensating for this defect [20–23]. However, these generated 2D Airy beam arrays take less or no account of the coherence or incoherence of the constituent beamlets. The average intensities of both phase-locked and nonphase-locked Airy beam array propagating through atmospheric turbulence are derived based on the extended Huygens–Fresnel principle [24]. In fact, the incoherent combination beam array demonstrates more favorable features in some applications such as in scintillation reduction of free space optical communication [25]. By using the "self-bending feature" of Airy beams, the constituent beamlets propagate through independent regions of turbulence and just overlap at the receiver plane. It is found that, by the numerical simulation, the scintillation of an incoherent Airy beam array can significantly be reduced to the theoretical minimum [26]. To deeply understand the scintillation reduction mechanism of Airy beam array propagation through atmospheric turbulence, the generation method of the incoherent combination of a 2D Airy beam array (ICCAB) and the coherent combination of a 2D Airy beam array (CCAB), and experiments to illustrate their scintillation characteristics are desirable.

In this paper, we focus on, through experiments, the incoherent and coherent combination of 2D Airy beam arrays and demonstrate their scintillation properties in atmospheric turbulence. A simple method using only one expended laser beam to generate both an incoherent and a coherent combination of

a two-beamlet 2D Airy beam array is developed. This is realized by using a phase display device in the optical system to directly destroy the coherence between the constituent two beamlets. The corresponding numerical calculation of the generation method using the phase screen method is illustrated. In addition, the scintillation characteristics of ICCAB and CCAB in atmospheric turbulence are experimentally analyzed.

2. PRINCIPLE DESCRIPTION

In this section, we begin with a brief theoretical description of the mathematical model of ICCAB and CCAB. Then, the generation method of ICCAB and CCAB and the corresponding numerical calculation using the phase screen method are demonstrated.

A. Mathematical Model

A centrosymmetric Airy beam array consisting of n 2D finite energy Airy beamlets can be described as [24]

$$\phi = \sum_{m=1}^{n} \phi_m, \tag{1}$$

where ϕ_m is the mth electric field envelope of the symmetric Airy beam array, $m = 1, 2, 3 \ldots n$, n labels the number of the Airy beamlets, the mth beamlet of the beam array can be expressed as

$$\begin{aligned}\phi_m(s_{mx}, s_{my}, \xi) = {} & Ai\left[s_{mx} - \left(\frac{\xi}{2}\right)^2 + ia\xi\right] \\ & \times Ai\left[s_{my} - \left(\frac{\xi}{2}\right)^2 + ia\xi\right] \\ & \times \exp\left(as_{mx} - \frac{a\xi^2}{2} - \frac{i\xi^3}{12} + ia^2\frac{\xi}{2} + is_{mx}\frac{\xi}{2}\right) \\ & \times \exp\left(as_{my} - \frac{a\xi^2}{2} - \frac{i\xi^3}{12} + ia^2\frac{\xi}{2} + is_{my}\frac{\xi}{2}\right),\end{aligned} \tag{2}$$

where a is the decay factor, which is a small positive parameter associated with the effective aperture of the system, ξ is a normalized propagation distance, and (s_{mx}, s_{my}) is dimensionless transverse coordinates of mth Airy beamlet is given by

$$\begin{cases} s_{mx} = \dfrac{x\cos(\theta_m) + y\sin(\theta_m) + c}{x_0}, \\ s_{my} = \dfrac{y\cos(\theta_m) - x\sin(\theta_m) + c}{y_0}, \\ \theta_m = \dfrac{m-1}{n}2\pi + \dfrac{3}{4}\pi, \end{cases} \tag{3}$$

where x_0, y_0 are the arbitrary transverse scale, taking $x_0 = y_0$, as we consider only the symmetric 2D finite energy Airy beams in this paper. θ_m is the rotary angle of the mth beamlet in the Cartesian coordinates, and c is the transverse displacement parameter of the beamlet from the origin.

The intensity distributions of ICCAB (I_{nc}) and CCAB (I_c) at the propagation distance ξ can be described as follows, respectively:

$$I_{nc} = \sum_{m=1}^{n} (\phi_m(s_{mx}, s_{my}, \xi) \times \phi_m^*(s_{mx}, s_{my}, \xi)), \tag{4}$$

$$I_c = \left(\sum_{m=1}^{n} \phi_m(s_{mx}, s_{my}, \xi)\right) \times \left(\sum_{m=1}^{n} \phi_m^*(s_{mx}, s_{my}, \xi)\right). \tag{5}$$

B. Numerical Calculation of Generation Method

The Fourier transform method was first used by Siviloglou to experimentally generate an Airy beam [1], putting the Fourier transform of the Airy beam (a cubic-phase mask) in the phase plane and then using a Fourier lens to inverse the Fourier transform; thus, the Airy beam is generated in an image plane as shown in Fig. 1.

For an Airy beam array, the phase mask for the mth Airy beamlet is expressed by

$$\Phi_m = \mathrm{Mod}_{2\pi}[\mathrm{Ang}(\varphi_m + \varphi_{Fm})], \tag{6}$$

where $\mathrm{Mod}_{2\pi}(\cdot)$ stands for modulation of the phase value within 0 to 2π, $\mathrm{Ang}(\cdot)$ denotes taking the phase value of a complex element, $\varphi_m = \mathcal{F}(\phi_m(s_{mx}, s_{my}, 0)$ is the Fourier transform of the mth beamlet, and $\mathcal{F}$ represents the Fourier transform. Instead of a Fourier lens in the optical system, we use a Fresnel lens phase function to generate the Airy beam, described as $\varphi_{Fm} = 2\pi \times [(x + c_m)^2 + y^2] \times z/\lambda f^2$ [27]; z is the displacement of the image relative to the focal plane of the lens with focal length f, and c_m stands for the transverse displacement from the origin of the mth beamlet.

In this paper, we focus on the incoherent and coherent combination method of an Airy beam array, thus taking the corresponding parameter $n = 2$. The final phase mask for a two-beamlet Airy array can be expressed by

$$\Phi = \begin{cases} \Phi_1 = \mathrm{Mod}_{2\pi}[\mathrm{Ang}(\varphi_1 + \varphi_{F1})] & x < 0 \\ \Phi_2 = \mathrm{Mod}_{2\pi}[\mathrm{Ang}(\varphi_2 + \varphi_{F2})] & x > 0 \end{cases}. \tag{7}$$

To show that the generation method is accurate, the multiple-phase screen method [26] is used for independent numerical calculation to simulate the combination and propagation of the Airy beam array. In simulation, the input beam is a Gauss beam in which the beam waist is 50 mm at a distance of

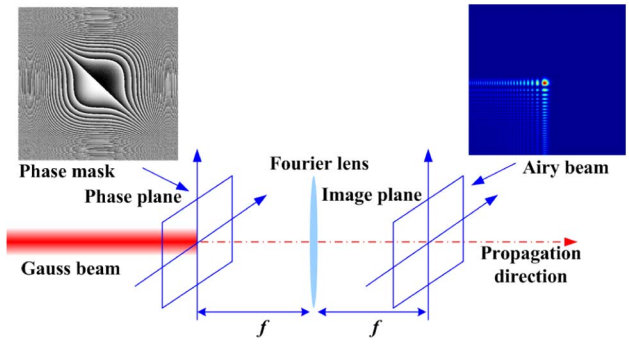

Fig. 1. Schematic of a conventional optical Fourier system to generate an Airy beam.

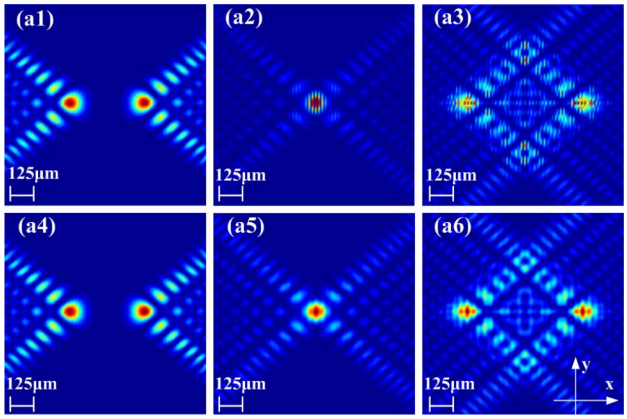

Fig. 2. Numerical simulations of ICCAB and CCAB at different distances. a1 to a3 are the combination process for CCAB, and a4 to a6 are the combination process for ICCAB. (a1, a4), (a2, a5), and (a3, a6) are the corresponding intensity patterns at 0.19 m, 0.2 m, and 0.215 m, respectively.

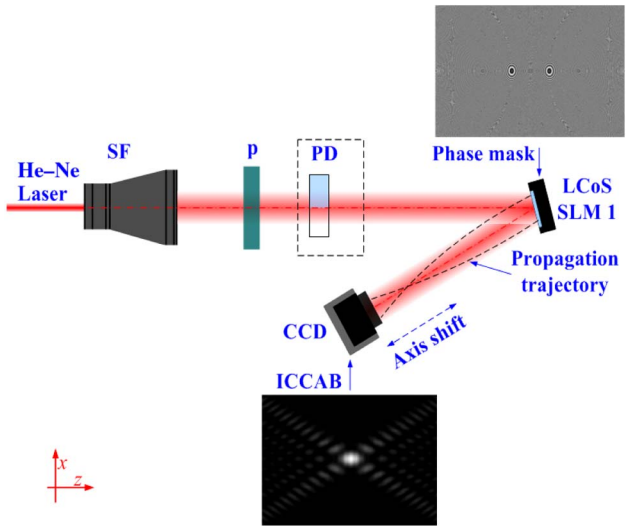

Fig. 3. Schematic of the experimental setup to generate ICCAB and CCAB. Where, He–Ne laser is a collimated 632.8 nm laser, SF is the spatial filter, P is a polarizer, PD is a phase-delay device, LCoS SLM 1 is a liquid crystal on silicon spatial light modulator, the black-dotted line denotes the propagation trajectory of the Airy beam array, and the blue-dotted arrow represents the axially scanning direction of the CCD camera.

−0.5 m. The only phase screen introduced to the simulation is calculated according to Eq. (7) at origin (0 m). The other parameters are taken as follows: the arbitrary transverse scale x_0, y_0 is 26 μm, the decay factor a is 0.03, the transverse displacement parameter c of the Airy beamlet is 1.94 mm, the focal length of the Fresnel lens is 190 mm, $c_1 = 3.84$ mm, $c_2 = -3.84$ mm, the wavelength is 632.8 nm, the simulated size is 1 mm × 1 mm, and the corresponding scale bar is 125 μm.

Figures 2(a1–a6) are the simulated propagation dynamics of ICCAB and CCAB. It is noted that both ICCAB and CCAB come into one main lobe during their propagation at a distance of 0.2 m due to its self-bending feature, as seen in Figs. 2(a2, a5). We define this propagation distance as the converged plane in this paper. Figures 2(a1, a4) are the intensity patterns of ICCAB and CCAB at a distance of 0.19 m. And Figs. 2(a3, a6) are the intensity patterns of ICCAB and CCAB at a distance of 0.215 m.

Clearly, the main lobe of CCAB in Fig. 2(a2) has the obvious interference fringe along the transverse shift axis; however, the main lobe of ICCAB in Fig. 2(a5) without an interference fringe has a symmetric Gaussian-like intensity distribution. This is the obvious characteristic between CCAB and ICCAB. The reason for this difference is mainly the coherence reduction of the constituent beamlets. When the two beamlets are incoherent, the intensity of ICCAB is only a combination of the intensity of each constituent beamlets numerically. In addition, it is also noted that before the converged plane, the intensity pattern of the constituent beamlets in Figs. 2(a1, a4) are same with each other and without the interference fringe. After the converged plane seen in Figs. 2(a2, a3, a5, a6), the intensity pattern of CCAB always demonstrates the interference fringe along the transverse shift direction. However, the intensity pattern of ICCAB does not demonstrate the interference fringe.

3. EXPERIMENTAL GENERATION

The schematic of the experimental setup is shown in Fig. 3, and the operation of the optical system can be described as follows. First, a He–Ne laser (wavelength is 632.8 nm) goes through a spatial filter system to expand the Gauss beam waist to 50 mm. Then, the expanded beam passes through a polarizer, ensuring the polarized direction of the incident beam parallel with the long axis of the liquid crystal molecules. After that, a phase-delay (PD) device is placed into the optical system to reduce coherence of the two-part beams. Following that, the beam passes through a beam splitter and further gets to the LCoS SLM 1 [28,29], in which the incident angle is about 5°. And the incident beam is phase-only modulated by the LCoS SLM 1 through loading a phase mask of an Airy beam array onto the LCoS SLM 1. Finally, the combination process and propagation dynamics of a 2D Airy beam array can be captured by a CCD camera, which can axially scan near the converged plane.

To bring out the incoherent combination process in experiments, we use a laser with a spatial coherent length of only about 96 μm, and a PD device is adopted to reduce the coherence of the constituent beamlets; half of it is glass, and the other half of it is air, as seen in Fig. 3. The delayed optical path between the beamlets caused by the PD device is 3.12 mm, 32.5 times the spatial coherent length of laser beam, making sure that the constituent beamlets are almost incoherent. When the PD device moves out of the optical system, the two beamlets on the optical axis are coherent because their optical paths are equal.

The calculated phase mask [30] to generate ICCAB and CCAB according to Eq. (7) is illustrated in Fig. 4, sampled 1920 × 1080 pixels, and the calculated parameters are equal with the numerical simulation in Section 2.B. The phase mask is obtained by superimposing a phase mask of a two-beamlet Airy beam array in Fig. 4(a) onto a phase mask of Fresnel lens in

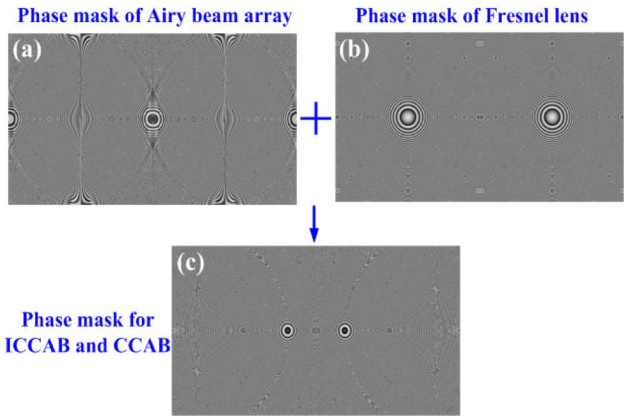

Fig. 4. Illustration of the phase mask for the laser combination of a 2D Airy beam array. (a) is the phase mask of a two-beamlet Airy beam array; (b) is the phase mask of Fresnel lens; and (c) is the superimposed phase mask to generate the CCAB and ICCAB, consisting of (a) and (b). Blank stands for grayscale value 0, and white stands for grayscale value 255.

Fig. 4(b). The LCoS SLM 1 used in the experiment is a reflective device, which is manufactured by Holoeye incorporation. The device panel has 1920 × 1080 pixels in a 15.36 mm × 8.64 mm array, with a pixel pitch of 8 μm × 8 μm and 87% fill factor.

In comparison, we respectively capture three intensity patterns of ICCAB and CCAB at three distances (0.19 m, 0.2 m, and 0.215 m) after LCoS SLM 1 corresponding to Figs. 5(b1, b4), 5(b2, b5), and 5(b3, b6), equal to the simulation. As predicted in the numerical calculation, the experimentally generated Airy beam arrays present the same incoherent and coherent properties and propagation dynamics. There are some excellent conclusions between the experimental results in Fig. 5 and the numerical simulations in Fig. 2. First, the intensity patterns in Fig. 5 are as similar as those in Fig. 2 at the three different propagation distances. However, it also can be seen that the intensities of the main lobes of Airy beams in Fig. 5(b6) is different, caused by the absorption and aberration of the glass in the PD device as

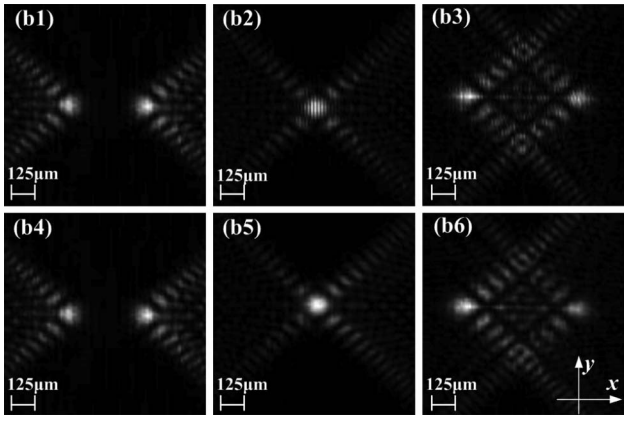

Fig. 5. Experimental results of ICCAB and CCAB. b1 to b3 are the combination process for CCAB; b4 to b6 are the combination process for ICCAB; and (b1, b4), (b2, b5), and (b3, b6) are the corresponding intensity patterns after the LCoS SLM 1 0.19 m, 0.2 m, and 0.215 m, respectively. The corresponding scale bar is also 125 μm.

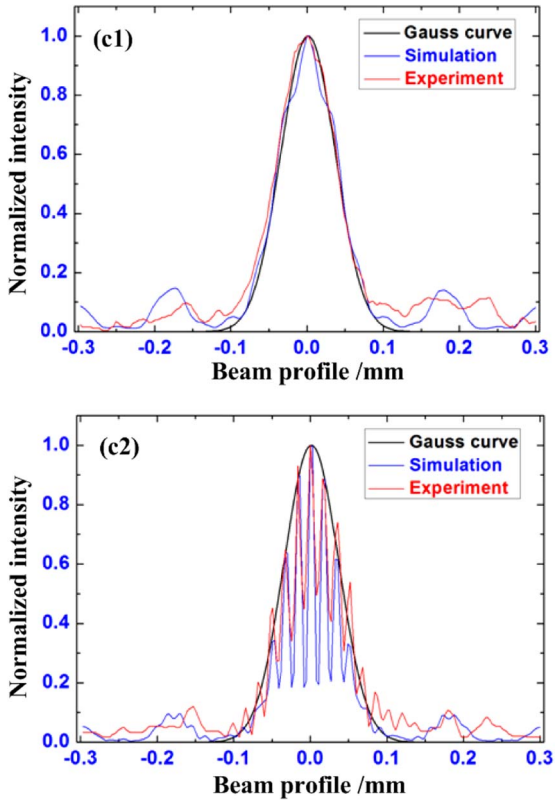

Fig. 6. Comparison of the normalized intensity profiles of experiment and numerical simulation along the transverse direction at distance 0.2 m. c1 stands for normalized intensity of CCAB, and c2 stands for normalized intensity of ICCAB.

seen in Fig. 3. The aberration of the glass especially will change the diffraction property of the generated Airy beamlet. Thus, with the propagation distance increasing, the intensities of the main lobes of the generated Airy beam array are different. Second, the main lobe of CCAB in Fig. 5(b2) has the obvious interference fringe along the transverse shift direction. And the main lobe of ICCAB in Fig. 5(b5) has the symmetric Gaussian-like intensity distribution. It obviously proves that the laser combination in Fig. 5(b5) is incoherent and in Fig. 5(b2) is coherent. Finally, after the converged plane as seen in Figs. 5(b2, b3, b5, b6), the intensity pattern of CCAB always demonstrates the interference fringe along the transverse shift direction. However, the intensity pattern of ICCAB does not demonstrate the interference fringe..

Figure 6 demonstrates the normalized intensity distributions of experimental and numerical simulation along the transverse direction at the converged plane. Figures 6(c1) and 6(c2) stand for normalized intensity of CCAB and ICCAB, respectively. It can be seen that the normalized intensity profile in experiments agree excellently with numerical simulation, both ICCAB and CCAB. In both cases as seen in Figs. 6(c1) and 6(c2), we found that the main lobe is symmetrical with a Gauss-like beam profile (the black solid line denotes the fitting Gauss curve). The spot sizes are all about 88 μm in the four cases, and the energy almost resides in them. From Figs. 5(b1) and 5(b4), the measurement spot sizes of the main lobes are

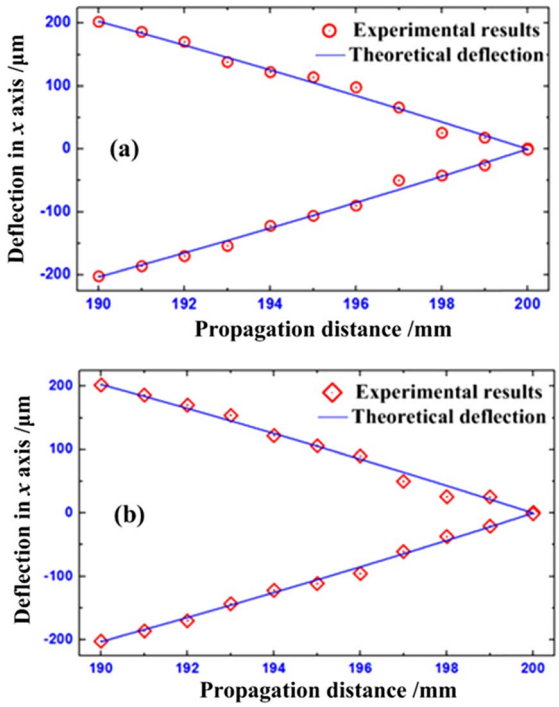

Fig. 7. Transverse accelerations in the x axis of the beamlets' main lobes of ICCAB and CCAB. (a) shows ICCAB and (b) shows CCAB, the blue curves depict the theoretical deflections, and the red rhombus or circles represent the experimental results.

almost 80 μm for both the incoherent and coherent Airy beam arrays. It is shown that the beamlet remains almost retain their original spot size (about 80 μm) for propagation at a 0.1 m distance (from 190 mm to 200 mm). Note that a Gaussian beam of this size (80 μm) would have diffracted 7.25 times in a 0.1 m propagation distance. It suggests that the constituted beamlets of ICCAB and CCAB remain almost diffraction-free properties during propagation along the z axis.

Figures 7(a) and 7(b) correspond to the x axis's transverse accelerations of the beamlets' main lobes of ICCAB and CCAB along the z axis, respectively. The blue curves depict the parabolic trajectory, which is well described by the theoretical relation $x = \lambda_0^2 z^2/(16\pi^2 x_0^3)$ [1], and the red rhombus or circles depict the measurement results. It can be seen that both ICCAB and CCAB clearly demonstrate the transverse acceleration in our experiment as seen in Fig. 7. As a result, after 0.1 m of propagation the beamlets of both ICCAB and CCAB almost experience a deflection of 202 μm, and the intensities of main lobes of both ICCAB and CCAB set together at a distance of 0.2 m.

To demonstrate the self-healing properties of both ICCAB and CCAB, we block one of the main lobes at a distance of 0.19 m as seen in Fig. 8. Also, we capture three intensity patterns of ICCAB and CCAB at three distances—0.19 m, 0.2 m, and 0.223 m—after LCoS SLM 1 corresponding to Figs. 8(c1, c4), 8(c2, c5), and 8(c3, c6), respectively. It depicts the reformation of the Airy beam array after propagation at a distance of 33 mm at distance 0.223 m. The self-healing of the blocked beamlet is apparent. The main lobes are reborn at the corner and are marked using the red arrows as shown in Figs. 8(c3) and 8(c6).

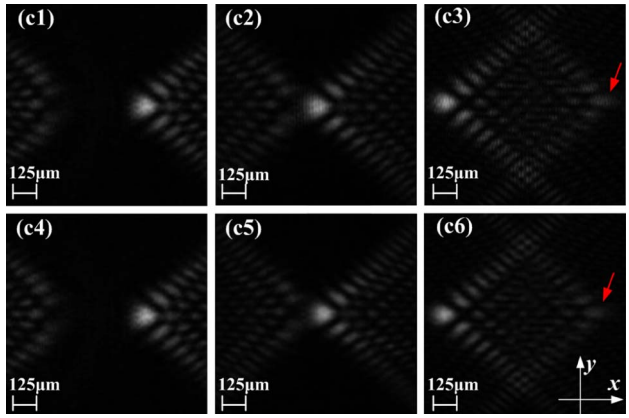

Fig. 8. Self-healing of CCAB and ICCAB with one of the main lobes is obstructed at distance 0.19 m; (c1) to (c3) stand for CCAB; (c4) to (c6) stand for ICCAB; and (c1, c4), (c2, c5), and (c3, c6) are the corresponding intensity patterns after the LCoS SLM 1 0.19 m, 0.2 m, and 0.233 m, respectively. The corresponding scale bar is 125 μm.

4. COMPARING SCINTILLATION CHARACTERISTICS OF ICCAB AND CCAB

Atmospheric turbulence, generated by a temperature differential between the earth's surface and the atmosphere, causes a fluctuation in received irradiance (including the temporal variation and spatial variation within a receiver aperture). The fluctuation in received irradiance resulting from propagation through atmospheric turbulence is commonly described as scintillation [31]. In this section, we briefly review two important atmospheric parameters used to describe atmosphere scintillation strength, and we focus on the scintillation characteristics of ICCAB and CCAB through a random medium, using an experimental method.

A. Experimental Parameters

Two important experimental parameters are of interest in this section. The Rytov variance for a plane wave is used as a measure of the strength of the scintillations as defined by [28]

$$\sigma_R = 1.23 C_n^2 k^{7/6} L^{11/6}, \tag{8}$$

where k is the wave number, L is the propagation distance, and C_n^2 is the refractive-index structure parameter. We generally define weak scintillations by the condition $\sigma_R < 1$, moderate scintillations by the condition $\sigma_R \approx 1$, and strong scintillations y the condition $\sigma_R > 1$. It is noted that Rytov variance is just a qualitative result to define the fluctuation conditions for a plane wave. In this paper, we use the Rytov variance to define the simulated experiment scintillation conditions for an Airy beam array, and it is also not a quantitative result for Airy beam array.

The on-axis scintillation index is adopted to characterize the scintillation strength of ICCAB and CCAB at the receiver plane in experiments [31],

$$\sigma^2(x, y, L) = \frac{\langle I^2(x, y, L)\rangle}{\langle I(x, y, L)\rangle^2} - 1, \tag{9}$$

where I is the instantaneous intensity, and $\langle\cdot\rangle$ denotes the ensemble average.

B. Setup

To experimentally show the scintillation characteristics of the incoherent and coherent 2D Airy beam arrays in turbulence, we adjust parts of the experimental setup in Fig. 3, as illustrated in Fig. 9. The components before and including LCoS SLM 1 are same with the setup in Fig. 3. The input laser is also an expanded Gauss beam with a wavelength of 632.8 nm and a waist of 50 mm. After LCoS SLM 1, another LCoS SLM 2 is put in the optical system with the incident angle, also about 5°. The purpose of SLM 2 is to introduce a random turbulence phase in real space where the Airy beam array propagation. The CCD camera (receive plane) is assigned after SLM 2 at 0.2 m. Thus, we can observe the main lobe intensity patterns of ICCAB and CCAB in turbulence at the converged plane and analyze scintillation characteristics of ICCAB and CCAB in different turbulent conditions. LCoS SLM 2 used in the experiment is a reflective liquid crystal spatial light modulator, which is built by Boulder Nonlinear Systems, including two 512×512 pixels.

The phase mask 1 in Fig. 9 is same with Fig. 4, and the calculated parameters are equal. The phase mask 2 is a random-phase screen generated by the multiple-phase screen method to simulate atmosphere turbulence, which is modulated over 0 to 2π and sampled 512×512 pixels to support the SLM 2. In experiments, we adjust the propagation distance and the refractive index structure constant C_n^2 to change the atmospheric strength. The other fixed parameters are as follows: the wavelength is 632.8 nm, and the size of the optical aperture is 0.3 m.

C. Experimental Results

We start with inputting the phase mask 2 with the fixed propagation distance of 2 km, and with varying C_n^2 0.125×10^{-14}, 0.25×10^{-14}, 0.5×10^{-14}, 1×10^{-14}, and 2×10^{-14}, respectively, corresponding to the Rytov variance 0.25, 0.5, 1, 2, and 4, respectively.

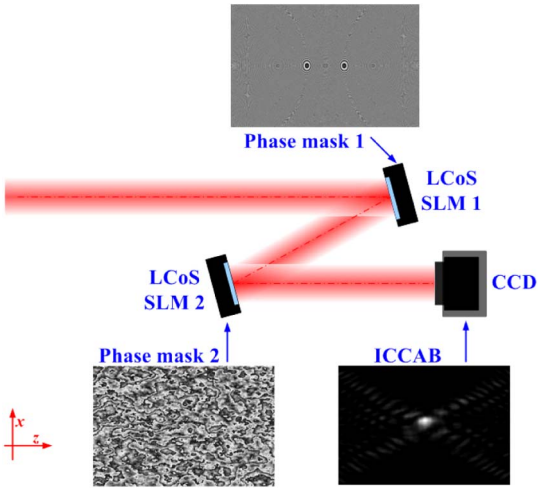

Fig. 9. Schematic of the experimental setup to demonstrate ICCAB and CCAB in turbulence. LCoS SLM 2 is a liquid crystal on silicon spatial light modulator; phase mask 1 is the same as Fig. 3; phase mask 2 is a random phase screen to simulate atmosphere turbulence; and the distance between the CCD and the LCoS SLM 1 is 0.2 m.

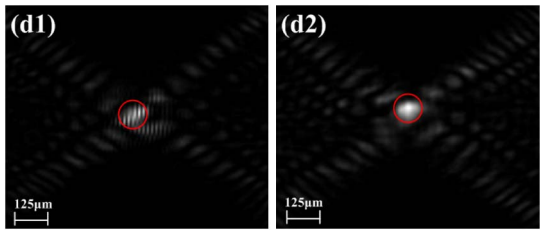

Fig. 10. Disturbed intensity patterns of ICCAB and CCAB at the receiver plane. d1 is CCAB and d2 is ICCAB, and the red circle marks the corresponding main lobe. Turbulence condition: the refractive index structure constant C_n^2 is 0.5×10^{-14} $m^{-2/3}$; the propagation distance is 2 km; and the corresponding Rytov variance is 1.

Figures 10(d1, d2) denote the captured intensity patterns of ICCAB and CCAB at the converged plane (0.2 m) in turbulent experiments. Compared to Figs. 2(a2, a5) and Figs. 5(b2, b5), the intensity patterns of ICCAB and CCAB in Fig. 10 are obviously disturbed by the random phase. However, the main lobes of ICCAB and CCAB maintain the intensity characteristics basically; they are marked using the red circle as shown in Fig. 10.

Figure 11 illustrates the obtained on-axis scintillation indices of ICCAB and CCAB under different scintillation conditions through varying turbulence strength C_n^2. It is shown that with the increase of the scintillation strength, the on-axis scintillation indices both of ICCAB and CCAB are increased together. However, the on-axis scintillation indices of ICCAB are all smaller than CCAB, whether in weak scintillation conditions ($C_n^2 = 0.125, 0.25 \times 10^{-14}$), moderate scintillation conditions ($C_n^2 = 0.5 \times 10^{-14}$), or strong scintillation conditions ($C_n^2 = 1, 2 \times 10^{-14}$). In weak scintillation conditions, the on-axis scintillation indices of ICCAB and CCAB are under 0.1. In moderate scintillation conditions, the on-axis scintillation indices of ICCAB and CCAB are about 0.15 and 0.17, respectively. And in moderate scintillation conditions, the on-axis scintillation indices of ICCAB and CCAB are up to the maximum of about 0.44 and 0.5, respectively.

We also present the on-axis scintillation indices of ICCAB and CCAB under different scintillation conditions with the

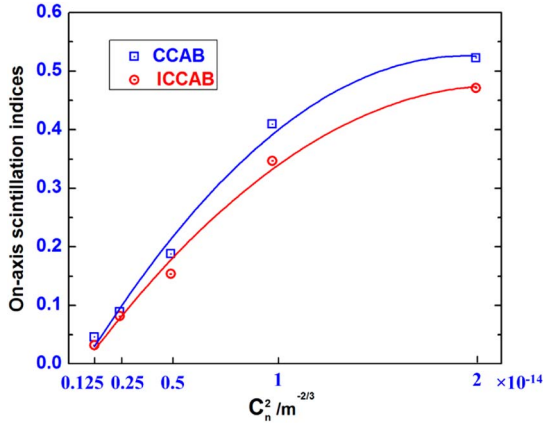

Fig. 11. On-axis scintillation indices of ICCAB and CCAB at the receiver plane with the fixed propagation distance and varying C_n^2 fluctuation conditions.

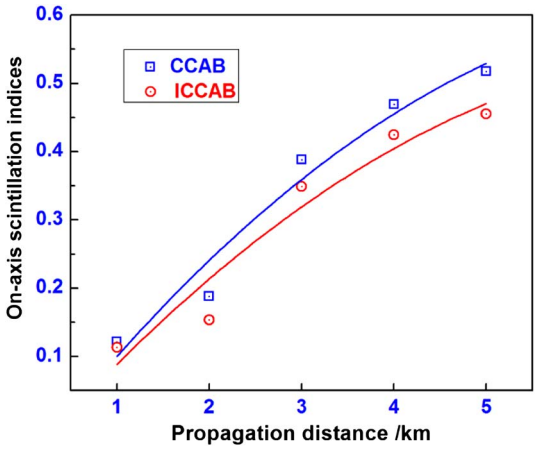

Fig. 12. On-axis scintillation indices of ICCAB and CCAB at the focal plane corresponding to a different propagation distance.

fixed $C_n^2 = 0.5 \times 10^{-14}$ and varying the propagation distance 1 km, 2 km, 3 km, 4 km, and 5 km respectively, corresponding to the Rytov variance 0.28, 1, 2.12, 3.59, and 5.41, respectively. The obtained on-axis scintillation indices of ICCAB and CCAB in experiments are shown in Fig. 12. It can be seen that as the propagation distance increases (the scintillation strength increasing), the on-axis scintillation indices of ICCAB and CCAB are increasing simultaneously. In weak scintillation conditions (1 km), the on-axis scintillation indices of ICCAB and CCAB are about 0.08 and 0.09, respectively. In moderate scintillation conditions (2 km), the on-axis scintillation indices of ICCAB and CCAB are about 0.15 and 0.18, respectively. And in strong scintillation conditions (5 km), the on-axis scintillation indices of ICCAB and CCAB reach the maximum of about 0.44 and 0.52, respectively.

One conclusion we can obtain from Figs. 11 and 12 is that the ICCAB has a smaller scintillation index than CCAB under the same scintillation condition. It can be interpreted as follows: without consideration of the coherence of an Airy beam array, each beamlet of the Airy beam array propagates through the relatively independent regions of experimental turbulence, producing their mutually uncorrelated intensity fluctuations and taking advantage of the statistical independence of fluctuations to reduce the on-axis scintillation indices. When the beamlets of the Airy beam array are incoherent, each beamlet is statistically independent of fluctuations even through the dependent regions of experimental turbulence. It strengthens the function of scintillation reduction of the beam array. If we consider the Airy beam array as a whole beam, due to the coherence reduction, ICCAB has the smaller beam coherence length, which can be seen as a partially coherent beam, while CCAB is a fully coherent beam. It is well known that partially coherent beams have a lower scintillation than fully coherent beams [25,32]. Thus, ICCAB has a smaller scintillation index than CCAB under the same scintillation condition.

5. CONCLUSIONS

A sample method to experimentally generate ICCAB and CCAB is presented in this paper. It is realized by using a PD device in the optical system to destroy the coherence of the used short spatial coherent length laser. The experimental results in Fig. 5 are exactly the same with the simulation results of ICCAB and CCAB in Fig. 2. After that, the scintillation characteristics of ICCAB and CCAB in turbulence are analyzed experimentally. It is shown that ICCAB has smaller scintillation indices than CCAB under different scintillation conditions. We think the successful generation method of ICCAB and a smaller scintillation index of ICCAB in turbulence are useful to reduce scintillation in the application of beam propagation through atmosphere turbulence. In addition, the influences of the coherent degree of the constituent Airy beamlets on the scintillation characteristics of the beam array under different turbulent conditions are worth more research.

Funding. National High Technology Research and Development Program of China (2015AA042402).

REFERENCES

1. G. A. Siviloglou and D. N. Christodoulides, "Accelerating finite energy Airy beams," Opt. Lett. **32**, 979–981 (2007).
2. J. Parravicini, P. Minzioni, V. Degiorgio, and E. DelRe, "Observation of nonlinear Airy-like beam evolution in lithium niobate," Opt. Lett. **34**, 3908–3910 (2009).
3. I. Dolev, T. Ellenbogen, and A. Arie, "Switching the acceleration direction of Airy beams by a nonlinear optical process," Opt. Lett. **35**, 1581–1583 (2010).
4. L. Li, T. Li, S. M. Wang, C. Zhang, and S. N. Zhu, "Plasmonic Airy beams generated by in-plane diffraction," Phys. Rev. Lett. **107**, 126804 (2011).
5. P. Zhang, S. Wang, Y. Liu, X. Yin, C. Lu, Z. Chen, and X. Zhang, "Plasmonic Airy beams with dynamically controlled trajectories," Opt. Lett. **36**, 3191–3193 (2011).
6. A. Minovich, A. E. Klein, N. Janunts, T. Pertsch, D. N. Neshev, and Y. S. Kivshar, "Generation and near-field imaging of Airy surface plasmons," Phys. Rev. Lett. **107**, 116802 (2011).
7. P. Zhang, J. Prakash, Z. Zhang, M. S. Mills, N. Efremidis, D. N. Christodoulides, and Z. Chen, "Trapping and guiding microparticles with morphing autofocusing Airy beams," Opt. Lett. **36**, 2883–2885 (2011).
8. I. D. Chremmos, Z. Chen, D. N. Christodoulides, and N. K. Efremidis, "Abruptly autofocusing and autodefocusing optical beams with arbitrary caustics," Phys. Rev. A **85**, 023828 (2012).
9. I. Chremmos, P. Zhang, J. Prakash, N. K. Efremidis, D. N. Christodoulides, and Z. Chen, "Fourier-space generation of abruptly autofocusing beams and optical bottle beams," Opt. Lett. **36**, 3675–3677 (2011).
10. N. Efremidis and D. Christodoulides, "Abruptly autofocusing waves," Opt. Lett. **35**, 4045–4047 (2010).
11. D. G. Papazoglou, N. K. Efremidis, D. N. Christodoulides, and S. Tzortzakis, "Observation of abruptly autofocusing waves," Opt. Lett. **36**, 1842–1844 (2011).
12. N. K. Efremidis, V. Paltoglou, and W. von Klitzing, "Accelerating and abruptly autofocusing matter waves," Phys. Rev. A **87**, 043637 (2013).
13. J. Li, X. Fan, W. Zang, and J. Tian, "Vacuum electron acceleration driven by two crossed Airy beams," Opt. Lett. **36**, 648–650 (2011).
14. Z. Zheng, B. Zhang, H. Chen, J. Ding, and H. Wang, "Optical trapping with focused Airy beam," Appl. Opt. **50**, 43–49 (2011).
15. J. Baumgartl, M. Mazilu, and K. Dholakia, "Optically mediated particle clearing using Airy wavepackets," Nat. Photonics **2**, 675–678 (2008).
16. A. M. Rubenchik, M. P. Fedoruk, and S. K. Turitsyn, "The effect of self-focusing on laser space-debris cleaning," Light Sci. Appl. **3**, e159 (2015).

17. S. S. Kou, G. Yuan, Q. Wang, L. Du, E. Balaur, D. Zhang, D. Tang, B. Abbey, X. Yuan, and J. Lin, "On-chip photonic Fourier transform with surface plasmon polaritons," Light Sci. Appl. **5**, e16034 (2016).
18. X. Chu, "Evolution of an Airy beam in turbulence," Opt. Lett. **36**, 2701–2703 (2011).
19. J. Broky, G. A. Siviloglou, A. Dogariu, and D. N. Christodoulides, "Self-healing properties of optical Airy beams," Opt. Express **16**, 12880–12891 (2008).
20. C. Hwang, D. Choi, K. Kim, and B. Lee, "Dual Airy beam," Opt. Express **18**, 23504–23516 (2010).
21. Z. Ren, Q. Wu, Y. Shi, C. Chen, J. Wu, and H. Wang, "Production of accelerating quad Airy beams and their optical characteristics," Opt. Express **22**, 15154–15164 (2014).
22. X. Wang, Q. Li, Z. Xiong, Z. Zhang, and Q. Wang, "Generation and scanning of Airy beams array by combining multiphase patterns," Appl. Opt. **52**, 3039–3047 (2013).
23. X. Yu, R. Li, S. Yan, B. Yao, P. Gao, G. Han, and M. Lei, "Experimental demonstration of 3D accelerating beam arrays," Appl. Opt. **55**, 3090–3095 (2016).
24. C. Chen, H. Yang, M. Kavehrad, and Z. Zhou, "Propagation of radial Airy array beams through atmospheric turbulence," Opt. Laser Eng. **52**, 106–114 (2014).
25. T. J. Schulz, "Optimal beams for propagation through random media," Opt. Lett. **30**, 1093–1094 (2005).
26. Y. Gu and G. Gbur, "Scintillation of Airy beam arrays in atmospheric turbulence," Opt. Lett. **35**, 3456–3458 (2010).
27. B. Ma, B. Yao, Z. Li, M. Lei, S. Yan, P. Gao, D. Dan, and T. Ye, "Generation of three-dimensional optical structures by dynamic holograms displayed on a twisted nematic liquid crystal display," Appl. Phys. B **110**, 531–537 (2003).
28. Z. Zhang, Z. You, and D. Chu, "Fundamentals of phase-only liquid crystal on silicon (LCOS) devices," Light Sci. Appl. **3**, e213 (2014).
29. W. Zhang, H. Zappe, and A. Seifert, "Wafer-scale fabricated thermopneumatically tunable microlenses," Light Sci. Appl. **3**, e145 (2016).
30. V. Bianco, P. Memmolo, M. Paturzo, A. Finizio, B. Jacidi, and P. Ferraro, "Quasi noise-free digital holography," Light Sci. Appl. **5**, e16142 (2016).
31. L. C. Andrews and R. L. Phillips, *Laser Beam Propagation Through Random Media* (SPIE, 2005).
32. O. Korotkova, , L. C. Andrews, and R. L. Phillips, "Model for a partially coherent Gaussian beam in atmospheric turbulence with application in lasercom," Opt. Eng. **43**, 330–341 (2004).